Vol. 48, No. 1 (2026) 21-38, DOI: 10.24874/ti.1983.07.25.09

Tribology in Industry

www.tribology.rs

RESEARCH

Performance of Microgrooves Textured Hydrodynamic Journal Bearing Under Contaminated Water Lubrication

Kai Feng Chua[a], Muhammad Noor Afiq Witri Muhammad Yazid[a, *], Zulhanafi Paiman[a], Syahrullail Samion[a], Zuraidah Rasep[b]

[a]*Faculty of Mechanical Engineering, Universiti Teknologi Malaysia, Skudai, 81310 Johor Bahru, Johor, Malaysia,*
[b]*Universiti Kuala Lumpur, Branch Campus Malaysian Institute of Industrial Technology (MITEC), Persiaran Sinaran Ilmu, Bandar Seri Alam, 81750 Johor Bahru, Johor, Malaysia.*

Keywords:

Hydrodynamic journal bearing
Contaminated water
Surface texture
Computational fluid dynamics
Taguchi grey relational analysis

* Corresponding author:

Muhammad Noor Afiq Witri Muhammad Yazid
E-mail: mnafiqwitri@utm.my

Received: 17 July 2025
Revised: 19 August 2025
Accepted: 27 September 2025

A B S T R A C T

This study investigates the effects of rectangular grooves on water-lubricated journal bearing (WLJB) using computational fluid dynamics (CFD) simulations. Optimization of groove parameters was performed using the Taguchi grey relational analysis (GRA) method. Key surface texture parameters considered were groove width, number of grooves, and groove locations, examined under two lubricants: pure and contaminated water. Optimized configurations were further evaluated at various rotational speeds and eccentricity ratios. Results reveal that surface texture configurations can both positively and negatively affect the load-carrying capacity (LCC) and frictional force of journal bearings. The optimal configuration was identified as a groove width of 80 μm, four grooves and placement at diverging region, θ_C. In contrast, the worst configuration involved a groove width of 40 μm, six grooves and placement at minimum film thickness region, θ_B. The best texture configuration improved LCC by 33.62% and 43.33% while reducing friction force by 1.36% and 2.60% under pure and contaminated water lubrication, respectively. These findings demonstrate the effectiveness of CFD-guided GRA in optimizing surface textures for enhanced WLJB operation under environmentally sustainable lubrication.

1. INTRODUCTION

Journal bearings are fundamental components in various rotating machinery, providing support and stability to shafts in applications such as turbines, compressors, and propellers. These bearings operate under the principle of hydrodynamic lubrication, where a thin film of lubricant separates the journal and bearing surfaces to minimize friction and wear.

Traditionally, oil-based lubricants have been widely used due to their superior viscosity and load-carrying properties [1-2]. However, the use of oil in marine and industrial applications raises environmental and sustainability concerns, thereby encouraging the adoption of water-lubricated journal bearings (WLJB) as alternatives to conventional oil-lubricated systems. Water offers advantages such as biodegradability, cost-effectiveness, and a lower friction coefficient owing to its abundance and lower viscosity. Despite these benefits, its low viscosity and weaker film-forming ability present challenges in maintaining adequate load support [3], making WLJB more susceptible to wear under demanding operating conditions [4].

In marine and industrial environments, solid debris such as sand, rust, and metal particles can enter the lubrication system through clearances or external exposure [5]. Contaminants alter the lubricant's properties and increase surface interactions between the journal and bearing, leading to elevated wear rates and reduced service life [5-6]. Studies have shown that contamination causes surface indentation, abrasion, and frictional heating [7]. The severity of these effects depends on particle size, shape, and concentration, with larger and harder particles producing more significant surface degradation [7]. Boucherit et al. [8] reported that peak pressure, friction force, and surface deformation increase significantly, while rotor–bearing system stability decreases, in the presence of solid particles. Similarly, Sateesh Kumar et al. [9] observed that softer journal bearing materials generate more wear particles under contaminated hydrodynamic conditions, which further increases friction and wear. Beyond material properties, bearing geometry also influences wear rates under contamination. For example, [10] investigated contaminated water in marine strut propeller shaft bearings and highlighted geometry-dependent degradation.

To mitigate the adverse effects of contamination, researchers have explored various design modifications, particularly surface texturing. Surface texturing deliberately modifies bearing surfaces by introducing macro- or micro-features such as dimples or grooves [11], which enhance lubricant film formation and improve tribological performance. Dimples are localized cavities, while grooves are continuous channels cut along the bearing surface in axial, radial, or circumferential directions. Common dimple patterns include rectangular [12], triangular [13], circular [14] and elliptical [15], whereas common groove shapes include triangular [16], semi-circular [17] and rectangular [18]. Compared to dimples, groove textures in journal bearings have been less extensively studied [11].

Existing literature suggests that grooves can significantly influence journal bearing performance, but their effects depend on size, depth, distribution, and operating conditions. For example, Jin et al. [19] numerically simulated the effect of microgrooves on wear behaviour in WLJBs and found that grooves with a left-triangle bottom shape provided optimal wear and lubrication performance compared with semi-elliptical, rectangular, isosceles triangular, and right-triangular grooves. Marian et al. [20] reported that fully textured surfaces negatively affected LCC compared to smooth bearings. Conversely, Li et al. [12] reviewed that partial surface texturing enhances performance more effectively than full coverage.

In the context of surface-textured bearings with contaminated fluids, studies remain inconsistent. Dadouche and Conlon [21] found that lightly textured journal bearings performed better under contaminated lubrication. Litwin et al. [22] analysed the effects of polymer materials and groove textures on WLJB wear, while Litwin and Kropp [23] studied grooved bronze bushes with graphite under contaminated water lubrication, concluding that bush geometry had no significant impact on wear resistance.

Optimization techniques have been increasingly applied to surface texture design in hydrodynamic journal bearings (HJB). Shinde and Pawar [24] optimized groove textures using Taguchi Grey Relational Analysis (GRA) and reported improvements in LCC of 51.01% and a 9.84% reduction in frictional torque. Similarly, Liu et al. [25] applied Taguchi GRA to groove textures and achieved a 4.69% increase in maximum film pressure and a

0.42% reduction in friction loss. Ganesha et al. [26] optimized axial-grooved WLJBs through numerical analysis and found groove count to be the most influential parameter, followed by groove angle, attitude angle, and groove depth. Despite such progress, most prior studies considering contamination either optimized grooves with limited parameters [21] or examined only wear effects [22]. To the best of our knowledge, no prior work has simultaneously investigated rectangular grooves in WLJBs under contaminated conditions while applying a systematic optimization method (Taguchi GRA). This unique integration represents the novelty of the present study. Among groove modifications, transverse groove textures have shown promising results in improving hydrodynamic performance [27,28], which forms the focus of this study.

2. METHODOLOGY

2.1 Computational domain

Computational domain for the textured journal bearing (TB) was modelled as shown in Fig. 1. The dimensions were based on those reported by Gao et al. [29], with the attitude angle assumed to be positioned at the bottom. A summary of the journal bearing dimensions is presented in Table 1. Groove texture characteristics such as groove width, location, and number were selected based on dimensionless parameters using radial clearance as the reference size to assess hydrodynamic performance. Following [2], shallow textures were preferred over deep textures to achieve desirable performance. Accordingly, the groove depth was set to 20 µm for a radial clearance of 40 µm.

The separation distance between grooves was determined from groove width variations, following [30] and [31]. Distances were 3.47 mm, 3.45 mm, and 3.41 mm for groove widths of 20 µm, 40 µm, and 80 µm, respectively. Groove location selection was adapted from [32], while groove number variations were referred from [33]. Fig. 2 illustrates groove placements at the converging region (θ_A), minimum film thickness, h_{min} (θ_B), and diverging region (θ_C). Table 2 summarizes groove texture dimensions.

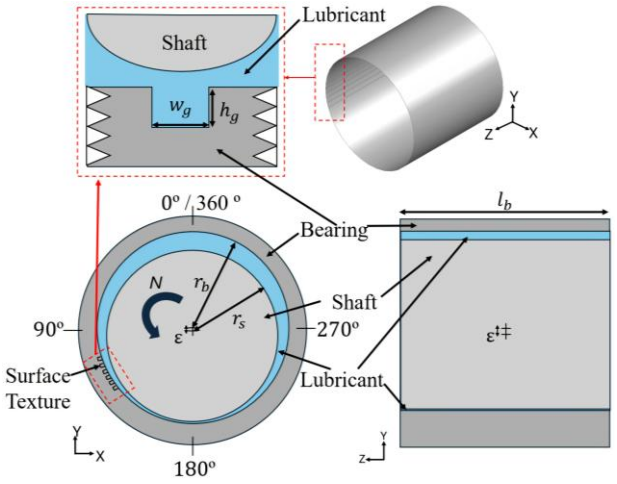

Fig. 1. Geometry definition of textured hydrodynamic journal bearing model.

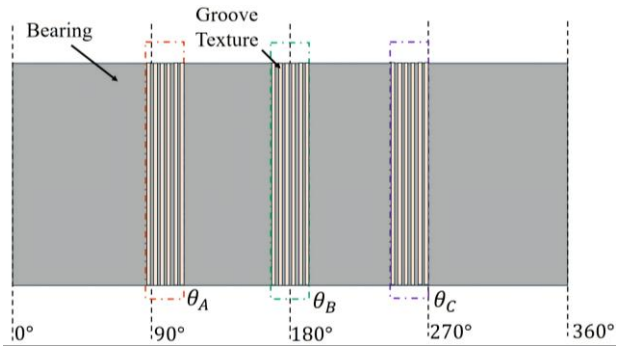

Fig. 2. Groove locations: converging, $\boldsymbol{\theta_A}$ (85^0 to 110^0), minimum film thickness, h_{min}, $\boldsymbol{\theta_B}$ (167.5^0 to 192.5^0) and diverging, $\boldsymbol{\theta_C}$ (245^0 to 270^0) regions.

Table 1. Summary of journal bearing CAD model.

Parameter	Value	Unit
Bearing inner radius, r_b	40.041	mm
Shaft radius, r_s	40.001	mm
Bearing length, l_b	80.21	mm
Radial clearance, c	0.04	mm
Length-diameter ratio, $L/2r_s$	1.0	-
Eccentricity ratio, ε	0.3, 0.5, 0.7	-
Rotational speed, N	200, 600, 1000	rpm
Bearing length, l_b	80.21	mm

Table 2. Rectangular groove texture parameters.

Parameter	Value	Unit
Groove depth, h_g	20	µm
Groove width, w_g	20, 40, 80	µm
Groove Locations	θ_A, θ_B , θ_C	-
Number of grooves, N_g	2, 4, 6	-

2.2 Meshing and boundary condition

Structured hexahedral meshes were generated for higher accuracy in smooth-flow regions and to better capture the flow field. Refined meshes were applied around texture cavities to improve precision in textured areas. The multizone method in ANSYS was used to create uniform hexahedral meshes across the fluid domain. Figs. 3(a) and 3(b) show refined meshes of the TB fluid domain.

Boundary conditions were set as follows: the inlet as a "pressure inlet," the outlet as a "pressure outlet" with gauge pressure of 0 Pa, the bearing wall as stationary with a no-slip condition, and the shaft wall as a moving wall with rotational motion. Fig. 3(c) illustrates the applied conditions.

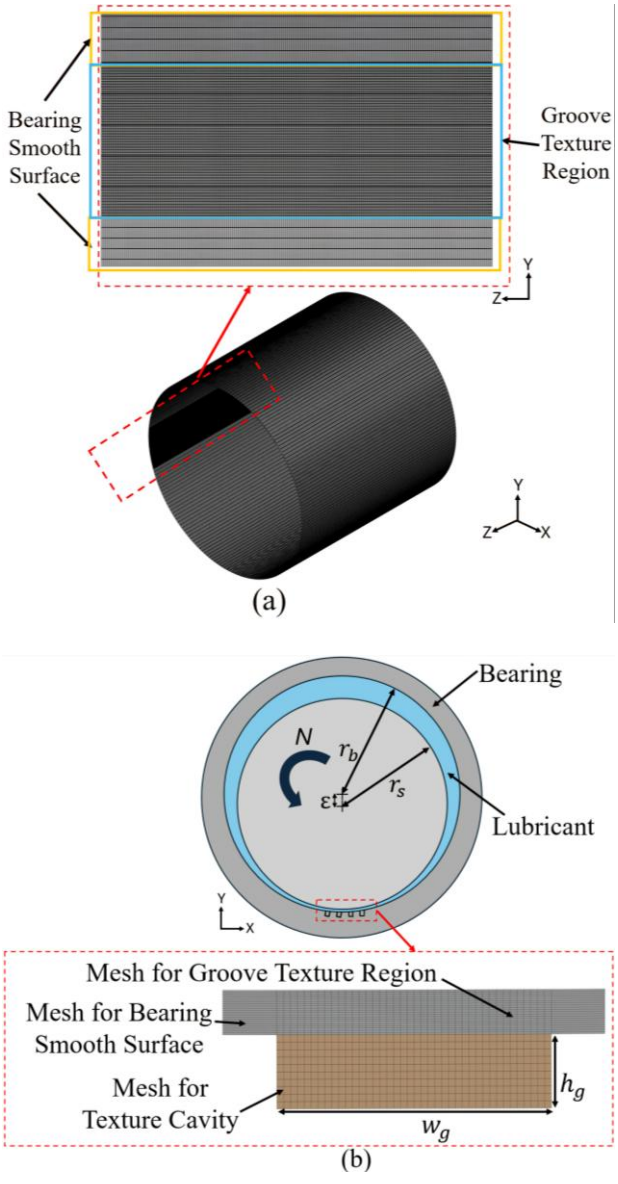

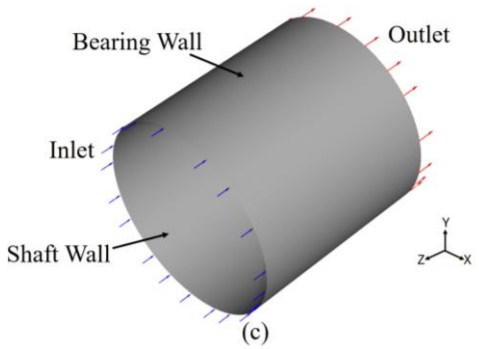

Fig. 3. (a) Refined meshes near texture region, (b) Detailed cavity mesh, (c) Boundary conditions.

2.3 Numerical Setup

ANSYS Fluent was used to perform CFD simulations with a multiphase cavitation model to capture interactions between water and vapor within the journal bearing [34]. The Zwart–Gerber–Belamri model was applied for cavitation prediction and convergence stability [35]. Particle concentration effects on cavitation threshold were assumed negligible, consistent with prior particle-laden flow studies [36-38]. Thus, saturation vapor pressure of water was set at a constant 2340 Pa for both pure and contaminated water lubricants.

The Reynolds number, based on bearing clearance, was sufficiently low even at 1000 rpm, justifying a laminar flow assumption. For contaminated water (CW), fluid–particle interactions are commonly modelled using the Discrete Phase Model (DPM) or Dense DPM (DDPM). For example, Zhou et al. [39] used DPM to simulate particle phases in hydrodynamic bearings, while [40] applied DDPM for WLJBs with dynamic particle effects.

Due to high computational cost and extended runtimes, neither DPM nor DDPM was employed. Instead, contamination effects were indirectly accounted for by modifying thermophysical properties of the water, specifically, density and viscosity, to reflect the presence of suspended particles. The effective density, ρ_{eff} and effective viscosity, μ_{eff} of the contaminated fluid were calculated using equation (1) and (2), respectively, as functions of volume fraction, φ , fluid density, ρ_f, particle density, ρ_p, and fluid viscosity, μ_f following the approach by [41]. In this study, two cases were considered: pure water (PW) with 0 vol.%, and

highly contaminated water (CW) with 24.8 vol.%, which is within the concentrations used in previous studies [8,23].The calculated ρ_{eff} and μ_{eff} for 24.8 vol.% CW were 1407.8 kg·m^{-3} and 0.015 kg·m^{-1}s^{-1}, respectively.

$$\rho_{eff} = (1-\varphi)\rho_f + \varphi\rho_p \quad (1)$$

$$\frac{\mu_{eff}}{\mu_f} = 1 + 56.5\varphi \quad (2)$$

In another note, SIMPLEC scheme was used for pressure–velocity coupling, and second-order upwind discretization was applied for spatial discretization. The residual of the z-momentum equation is stabilized below 1×10^{-5}, but the continuity and other momentum components stabilized at 1×10^{-3} after 1000 iterations. Table 3 summarises thermophysical properties and cavitation parameters used in the CFD simulation.

Table 3. CFD simulation parameters and properties.

Parameter	Value	Unit
Temperature of water	20	ºC
Saturation water vapour pressure	2340	Pa
Saturation density of water	998.2	kg/m^3
Saturation density of water vapor	0.5542	kg/m^3
Dynamic viscosity of water	1×10^{-3}	Pa s
Dynamic viscosity of water vapor	1.34×10^{-5}	Pa. s
Bubble radius, R_b	10^{-6}	m
Evaporation coefficient, C_{evap}	50	-
Condensation coefficient, C_{cond}	0.01	-
Nucleation site volume fraction	5×10^{-4}	-
Particle concentration of PW	0	vol%
Particle concentration of CW	24.8	vol%
Effective density of CW, ρ_{eff}	1407.68	kg/m^3
Effective viscosity of CW, μ_{eff}	0.0150	Pa s

2.4 Load-carrying capacity and frictional force

The load-carrying capacity (LCC) of a journal bearing indicates the maximum load that the bearing can support. The equation to calculate LCC [42-43] is defined as:

$$\text{LCC} = \sqrt{F_x^2 + F_y^2} \quad (3)$$

where,

$$F_x = \int_0^1 \int_0^{2\pi} pr\cos\theta \, d\theta dz \quad (4)$$

$$F_y = \int_0^1 \int_0^{2\pi} pr\sin\theta \, d\theta dz \quad (5)$$

where p is oil film pressure, r is the radius of the shaft and θ is circumferential angle of the shaft. Meanwhile, the frictional force, F_f [44] acting on the shaft is defined as:

$$F_f = -\iint_A \tau r d\theta dz \quad (6)$$

where τ is wall shear stress.

2.5 Surface texture optimization

Taguchi Grey Relational Analysis (GRA) was employed to determine optimal and worst-performing texture parameters under PW and CW lubrication. The dependent variables considered in the GRA were LCC and F_f. Normalized values for LCC (larger is better), is given in equation (7), while the normalized values for F_f (smaller is the better), is provided in equation (8) [45-46]:

$$X_i(k) = \left(\frac{x_i - x_{min}}{x_{max} - x_{min}}\right) \quad (7)$$

$$X_i(k) = \left(\frac{x_{max} - x_i}{x_{max} - x_{min}}\right) \quad (8)$$

where x_{min} is minimum value and x_{max} is maximum value for sequence.

Grey relational coefficients are then computed using equation (9).

$$\gamma_i(k) = \left(\frac{\Delta_{min} + \xi\Delta_{max}}{\Delta_i + \xi\Delta_{max}}\right) \quad (9)$$

where $\Delta_i = (X_i)_{max} - X_i$, $0 < \xi \leq 1$

After calculating the grey relational coefficients, grey relational grade (GRG) was then computed to identify the best configuration using equation (10).

$$GRG_i = \frac{1}{n}\sum_{k=1}^{n} \gamma_i(k) \quad (10)$$

where n is the quantity of performance characteristics.

A response table for the mean and ANOVA were tabulated to compare the relationship among these parameters. For the location labelling, θ_A, θ_B and θ_C are labelled as 1, 2 and 3, respectively in the optimization. Table 4 summarizes the input parameters and levels used for the texture parameters optimization, whereas Table 5 lists the experiment design for optimization. Optimization was performed at constant rotational speed of 1000 rpm and eccentricity of 0.7.

Table 4. Input parameters for optimization.

Level	Width (μm)	Location	No. of Grooves
1	20	1	2
2	40	2	4
3	80	3	6

Table 5. Experiment design for optimization.

Exp	Width (μm)	Location	No. of Groove
1	20	3	2
2	20	2	2
3	20	1	2
4	40	3	2
5	40	2	2
6	40	1	2
7	80	3	2
8	80	2	2
9	80	1	2
10	20	3	4
11	20	2	4
12	20	1	4
13	40	3	4
14	40	2	4
15	40	1	4
16	80	3	4
17	80	2	4
18	80	1	4
19	20	3	6
20	20	2	6
21	20	1	6
22	40	3	6
23	40	2	6
24	40	1	6
25	80	3	6
26	80	2	6
27	80	1	6

2.6 Verification and validation study

In this study, verification and validation studies were conducted to ensure the reliability and accuracy of the numerical settings and model incorporated in the simulation. The computational domain of TB has been discretized with a structured hexahedral mesh added with sizing options for controlling the mesh density. A grid independence study was conducted to determine the optimal grid spacing by comparing three different cell elements: 41500 (coarse), 320000 (medium), and 2560000 (fine) elements. Hydrodynamic moment that is calculated by multiplying shaft frictional force of Eq. (6) with shaft radius. The error between medium and fine grids was only 0.0001%, confirming the adequacy of the medium mesh. In this study, the fine mesh was used for the fluid domain of hydrodynamic journal bearing.

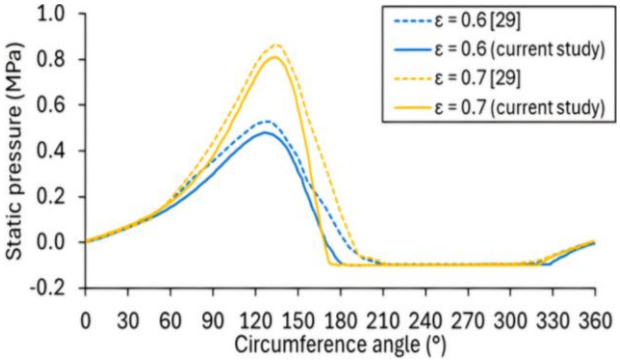

Fig. 4. Comparison of pressure distribution of present study and published data [29] at eccentricity ratio of 0.6 and 0.7.

Published data [29], under the same parameters which are eccentricity ratios 0.6 and 0.7, rotational speed 1500 rpm with water as lubricant have been considered for validation. Fig. 4 shows comparison between pressure for plain journal bearing (PB) by the present study and published data at eccentricity ratios 0.6 and 0.7. For eccentricity 0.6, peak pressure of present study is 0.480 MPa at 111.6° whereas the peak pressure of published data is 0.497 MPa at 128.29°. The percentage difference for peak pressure was determined at 3.45%. Meanwhile, peak pressure for eccentricity 0.7 of present study is 0.811 MPa at 118.8° whereas peak pressure of published data is 0.869 MPa at 133.37°. The percentage difference for peak pressure was determined at 6.69%. Since the differences were below 7% with the overall pattern and magnitude of pressure distribution are consistent, results were considered validated, and the present studies are reliable compared to [29].

3. RESULT AND DISCUSSION

3.1 Surface texture optimization

Optimization of texture parameters was conducted using GRA to identify the best and worst configurations under pure water (PW) and contaminated water (CW) lubrication. The dependent variables were the load carrying capacity (LCC) and frictional force (F_f), evaluated across groove widths, locations, and count. Table 6 presents optimization results for PW lubrication, while Table 7 presents result for CW lubrication. In both cases, green-highlighted rows indicate the optimal performance parameters (OPP), and orange-highlighted rows indicate the worst-performing parameters (WPP). The optimal configuration for the textured bearing (TB) involved a groove width of 80 μm, four (4) rectangular grooves and placement at θ_C. This configuration delivers higher LCC and lower F_f under both PW and CW lubrication. Conversely, the worst configuration featured a 40 μm groove width, six (6) rectangular grooves and placement at θ_B, resulting in lower LCC and higher F_f.

Table 6. Texture parameters optimization under PW lubrication.

Exp	LCC (kN)	F_f (kN)	Grade	Rank
1	1.5899	0.003090	0.7431	5
2	1.3817	0.003222	0.3828	26
3	1.4850	0.003118	0.5506	19
4	1.5884	0.003098	0.7253	6
5	1.4596	0.003068	0.6290	15
6	1.5240	0.003098	0.6235	16
7	1.6253	0.003060	0.9101	3
8	1.3279	0.003097	0.4946	21
9	1.5147	0.003098	0.6135	17
10	1.6037	0.003040	0.9146	2
11	1.5320	0.003199	0.5164	20
12	1.5082	0.003068	0.6706	11
13	1.5891	0.003044	0.8676	4
14	1.4289	0.003264	0.3859	25
15	1.5022	0.003061	0.6850	8
16	1.5946	0.003035	0.9164	1
17	1.4457	0.003247	0.4057	23
18	1.4943	0.003059	0.6824	9
19	1.5531	0.003155	0.5841	18
20	1.4697	0.003203	0.4507	22
21	1.5456	0.003087	0.6735	10
22	1.4873	0.003069	0.6471	13
23	1.3187	0.003216	0.3606	27
24	1.5947	0.003120	0.7034	7
25	1.5583	0.003114	0.6439	14
26	1.4059	0.003208	0.4046	24
27	1.5401	0.003086	0.6673	12

Table 7. Texture parameters optimization under CW lubrication.

Exp	LCC (kN)	F_f (kN)	Grade	Rank
1	18.3730	0.03618	0.6213	10
2	15.8084	0.03647	0.4773	16
3	15.3469	0.03653	0.4596	20
4	18.0122	0.03560	0.6835	5
5	15.7523	0.03687	0.4417	21
6	15.8727	0.03659	0.4678	19
7	20.0454	0.03685	0.7617	3
8	15.1764	0.03634	0.4736	17
9	16.1084	0.03662	0.4718	18
10	18.8642	0.03528	0.8163	2
11	18.8572	0.03836	0.5184	12
12	16.8451	0.03773	0.4249	23
13	18.6474	0.03551	0.7452	4
14	16.4806	0.03809	0.3956	24
15	16.9976	0.03693	0.4785	15
16	18.7220	0.03521	0.8239	1
17	17.0526	0.03783	0.4283	22
18	16.8427	0.03678	0.4831	14
19	19.1649	0.03680	0.6328	9
20	16.7756	0.03864	0.3859	25
21	17.4218	0.03677	0.5086	13
22	19.0587	0.03689	0.6145	11
23	15.6167	0.03823	0.3646	26
24	19.9557	0.03847	0.6605	7
25	19.2793	0.03643	0.6788	6
26	15.3318	0.03883	0.3370	27
27	18.8486	0.03640	0.6364	8

To determine parameter influence, LCC and F_f responses were further examined. Delta is calculated as the subtraction of largest mean value and smallest mean values, while the rank is determined based on delta (largest = rank 1; smallest = rank 3). The parameter with the highest rank has the most significant effect on the response. Table 8 and 9 summarize the response table for LCC mean under PW and CW lubrication, while Table 10 and 11 presents the response table for F_f mean under PW and CW lubrication. Overall, groove location had the greatest impact on both LCC and F_f, while groove width had the least impact.

Fig. 5(a) shows the maximum LCC was achieved at a 20 μm groove width. The maximum LCC occurred when grooves were placed at θ_C. For the number of grooves, the maximum LCC was obtained with four grooves. Fig. 5(b) shows that 20 μm and 80 μm provided similar LCC, while 40 μm lowered it. Besides that, the maximum LCC occurred when grooves were located at θ_C, while LCC increases with the number of grooves.

Fig. 6(a) shows that F_f decreased with groove width, reaching its minimum at 80 µm groove width. The minimum F_f was also observed at θ_C. Additionally, F_f increased with the number of grooves. Moreover, Fig. 6(b) shows that F_f was minimized with an 80 µm groove width (smaller is the better). The minimum F_f also occurred when grooves were located at θ_C. Like LCC, F_f increases when the number of grooves increases. In summary, both PW and CW exhibited similar trends; placing grooves at θ_B consistently resulted in lower LCC and higher F_f. A medium groove width of 40 µm generally lowered LCC, while 6 rectangular grooves produced higher F_f.

Table 8. Response table for LCC mean under PW.

Level	Width (µm)	Location	No. of Groove
1	1.519	1.523	1.5
2	1.499	1.419	1.522
3	1.501	1.577	1.497
Delta	0.02	0.158	0.025
Rank	3	1	2

Table 9. Response table for LCC mean under CW.

Level	Groove Width (µm)	Groove Location	No. of Groove
1	17.5	17.14	16.72
2	17.38	16.32	17.7
3	17.49	18.91	17.94
Delta	0.12	2.59	1.22
Rank	3	1	2

Table 10. Response table for F_f mean under PW.

Level	Width (µm)	Location	No. of Groove
1	3.131	3.088	3.105
2	3.115	3.191	3.113
3	3.111	3.078	3.14
Delta	0.02	0.113	0.034
Rank	3	1	2

Table 11. Response table for F_f mean under CW.

Level	Groove Width (µm)	Groove Location	No. of Groove
1	36.97	36.98	36.45
2	37.02	37.74	36.86
3	36.81	36.08	37.5
Delta	0.21	1.66	1.05
Rank	3	1	2

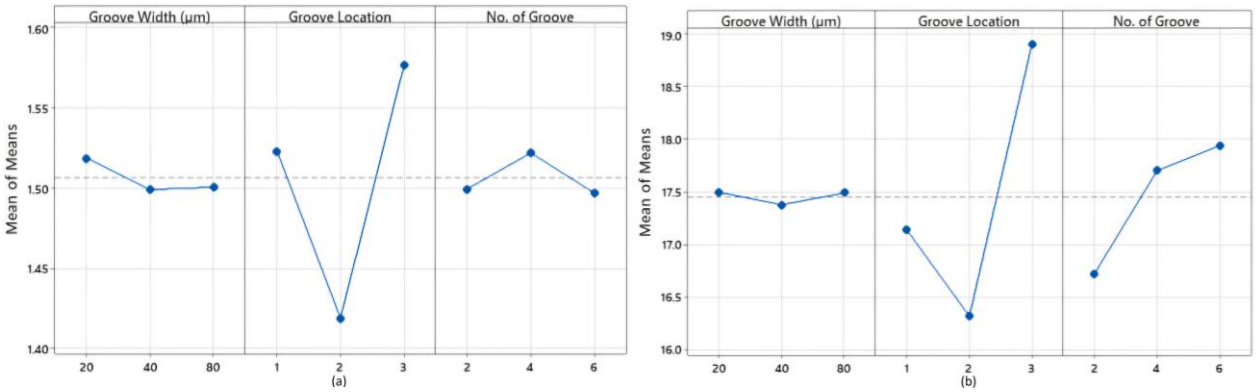

Fig. 5. Main effect plot for LCC mean under (a) PW lubrication (b) CW lubrication.

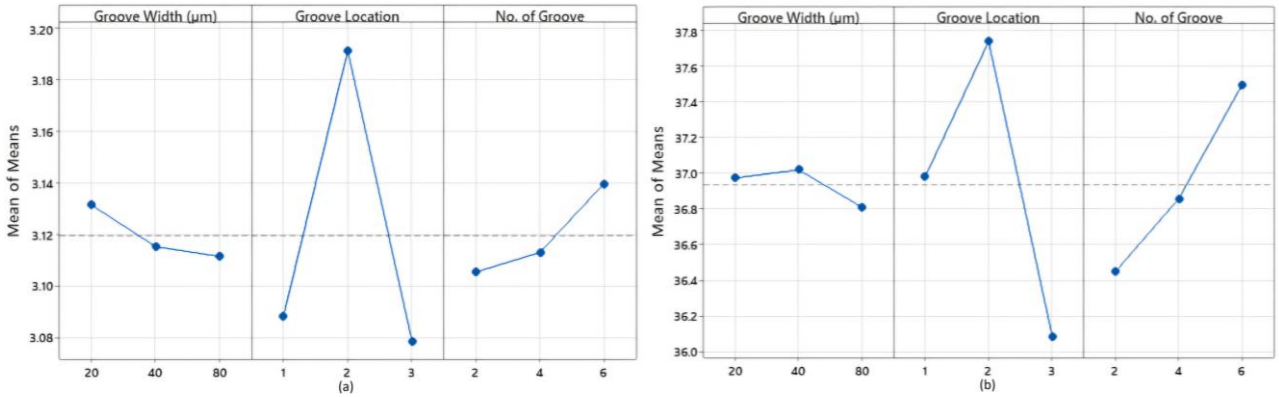

Fig. 6. Main effect plot for F_f mean under (a) PW lubrication (b) CW lubrication.

3.2 ANOVA for performance characteristics

Analysis of variance (ANOVA) quantified the contribution of each parameter to variability in LCC and F_f. Here, all factors had 2 degrees of freedom. Adjusted sums of squares (Adj SS), adjusted means squares (Adj MS), F-value and P-value were computed. Statistical significance was determined at the 95% confidence level ($P < 0.05$). Besides that, the percentage of contribution (%) was calculated by using equation (11).

$$\% = \frac{Adj\ SS}{Total\ Adj\ SS} \times 100\% \quad (11)$$

Tables 12 and 13 provide ANOVA results for LCC and F_f, respectively, under PW lubrication. Based on Table 12, the highest contribution on LCC with 66.09% is groove location, while the lowest contribution on LCC with 1.21% is groove width. The groove location was statistically significant for LCC under PW lubrication with a P-value of 1.0×10^{-5}. Based on Table 13, the highest contribution on F_f with 57.93% is groove location, while the lowest contribution on LCC with 1.66% is groove width. For F_f, the groove location was statistically significant under PW lubrication with a P-value of 6.4×10^{-5}.

Tables 14 and 15 provide ANOVA results for LCC and F_f, respectively under CW lubrication. Based on Table 14, the highest contribution on LCC with 51.02% is groove location, whereas the lowest contribution on LCC with 0.13% is groove width. For LCC in CW lubrication, groove location was statistically significant with a P-value of 1.7×10^{-4}. Based on Table 15, the highest contribution on F_f with 45.75% is groove location, whereas the lowest contribution on LCC with 0.81% is groove width. The groove location and number of grooves were statistically significant for F_f under CW lubrication with a P-value of 2.3×10^{-4} and 0.014, respectively.

Table 12. ANOVA for LCC under PW lubrication.

Source	DF	Adj SS	Adj MS	F-Value	P-Value	%
Groove Width (μm)	2	0.002	0.001	0.39	0.679	1.21
Groove Location	2	0.116	0.058	21.5	1.0e-5	66.09
No. of Groove	2	0.003	0.002	0.63	0.541	1.95
Error	20	0.054	0.003	-	-	-
Total	26	0.175	-	-	-	-

Table 13. ANOVA for F_f under PW lubrication.

Source	DF	Adj SS	Adj MS	F-Value	P-Value	%
Groove Width (μm)	2	0.002	0.001	0.47	0.635	1.66
Groove Location	2	0.071	0.035	16.26	6.4e-5	57.93
No. of Groove	2	0.006	0.003	1.35	0.283	4.80
Error	20	0.043	0.002	-	-	-
Total	26	0.122	-	-	-	-

Table 14. ANOVA for LCC under CW lubrication.

Source	DF	Adj SS	Adj MS	F-Value	P-Value	%
Groove Width (μm)	2	0.08	0.04	0.04	0.965	0.13
Groove Location	2	31.55	15.78	13.89	1.7e-4	51.02
No. of Groove	2	7.49	3.747	3.3	0.058	12.12
Error	20	22.72	1.135	-	-	-
Total	26	61.84	-	-	-	-

Table 15. ANOVA for F_f under CW lubrication.

Source	DF	Adj SS	Adj MS	F-Value	P-Value	%
Groove Width (μm)	2	0.218	0.109	0.23	0.796	0.81
Groove Location	2	12.36	6.178	13.12	2.3e-4	45.75
No. of Groove	2	5.015	2.508	5.33	0.014	18.57
Error	20	9.416	0.471	-	-	-
Total	26	27.00	-	-	-	-

3.3 Flow distribution inside journal bearing

Table 16 shows pressure and velocity contours within the texture cavity under PW and CW lubrications. A small region containing one groove was selected for comparison at ε =0.7 and N=1000 rpm. For OPP, lower pressures formed inside the cavity, suggesting cavitation is formed here. This coincided with higher hydrodynamic pressures opposite the cavity, improving LCC. Moreover, vortex structures were observed in both OPP and WPP; centred in WPP but shifted in OPP due to the wider cavity. Under CW lubrication, flow streamlines were smoother (less disturbed) due to its higher viscosity.

Table 16. Pressure and velocity contours for texture cavity under PW and CW.

Case	Pressure		Velocity	
	PW	CW	PW	CW
OPP			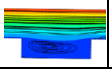	
WPP			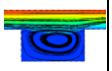	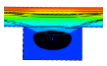
PB				
Scale	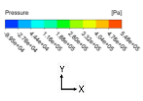	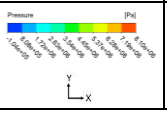	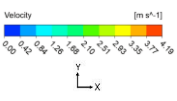	

3.4 Effect of eccentricity ratio and rotational speed

The effect of eccentricity ratio on OPP and WPP was studied at N = 1000 rpm, with plain bearings (PB) as benchmarks. Fig. 7 shows that LCC increased with eccentricity ratio. LCC for both OPP and WPP exceeded PB values under PW and CW. The OPP achieved maximum LCC of 1.59 kN and 18.72 kN, under PW and CW lubrication, respectively, at eccentricity ratio of 0.7. This is equivalent to 33.62% and 43.33% percentage improvement in LCC by OPP. Fig. 8 shows that F_f also increased with eccentricity ratio, with WPP consistently the highest. Under PW and CW lubrication, the WPP of TB reached a maximum F_f with a value of 0.0032 kN and 0.0382 kN, respectively, at an eccentricity ratio of 0.7. Besides that, F_f for OPP is increased at 0.3 and 0.5, but it was reduced F_f when the eccentricity ratio is 0.7 under both PW and CW with the values of 0.0030 kN and 0.0352, respectively. This is equivalent to 1.36% and 2.60% percentage reduction in frictional force by OPP under PW and CW, respectively, compared to PB.

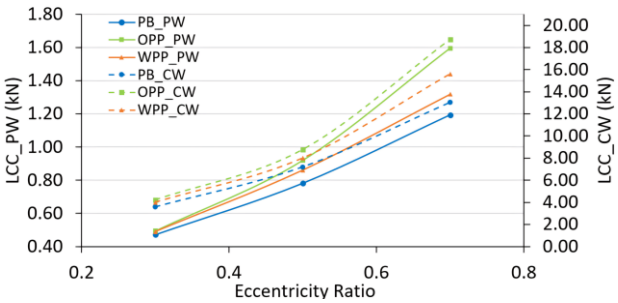

Fig. 7. LCC against eccentricity ratio under PW and CW lubrication.

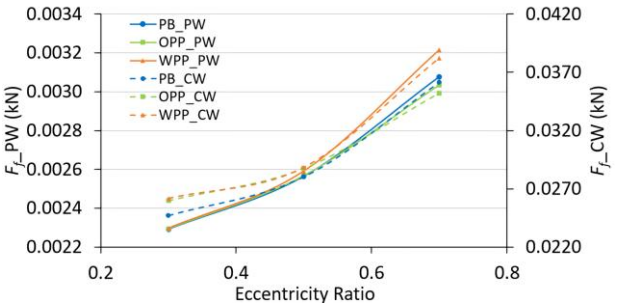

Fig. 8. F_f against eccentricity ratio under PW and CW lubrication.

Next, the effect of rotational speed on OPP and WPP were investigated for a fixed eccentricity ratio of 0.7 under PW and CW lubrication. PB under both PW and CW lubrication served as benchmarks. Referring to Fig. 9, there is an increasing trend for LCC when the rotational speed increases, while LCC for OPP and WPP is higher than the LCC of PB at all rotational speeds under both of lubrication. OPP of TB reached a maximum LCC of 1.59 kN and 18.72 kN under PW and CW lubrication, respectively, at rotational speed of 1000 rpm. The LCC of TB under CW lubrication is enhanced significantly because of its higher viscosity. Based on Fig. 10, F_f increases when the rotational speed increases for all the cases and WPP is the highest F_f for all the eccentricity ratios compared to the other cases. WPP of TB reached maximum F_f with the value of 0.0032 kN and 0.0382 kN, under PW and CW lubrication, respectively, at a speed of 1000 rpm. Besides that, F_f for OPP was increased at 200 rpm, but reduced when the speed is at 600 and 1000 rpm.

To better understand the underlying mechanisms driving the observed differences in performance between the optimal (OPP) and worst (WPP) configurations under varying eccentricity ratios and rotational speeds, distributions of pressure, wall shear stress (WS), and vapour volume fraction (VVF) were plotted along the circumference length of the bearing.

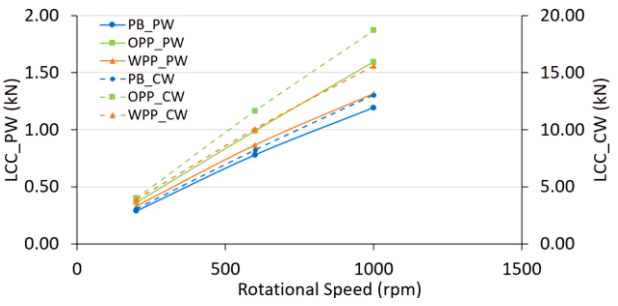

Fig. 9. LCC against rotational speed under PW and CW lubrication.

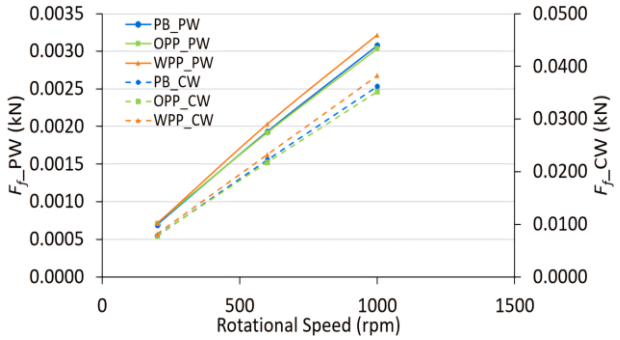

Fig. 10. F_f against rotational speed under PW and CW lubrication.

These visualizations offer critical insight into how texture geometry influences hydrodynamic film formation, shear behaviour, and cavitation characteristics. Based on Fig. 11(a), 11(d), 12(a), 12(d), 13(a) and 13(d), OPP had the highest peak pressure near converging region across eccentricity ratios and rotational speeds. The elevated pressure in the converging region causes the pressure in the diverging region to reduce in return, increasing the likelihood of cavitation. The generated peak pressure affects the LCC on the WLJB and this indicates an improved LCC by the increase in hydrodynamic pressure. Besides that, the increasing of peak pressure for OPP under PW were the most significant at ε = 0.7 and 1000 rpm (see Fig. 11(a)). This can be seen that full vapour inside texture cavity of OPP lower the wall shear stress in this region. This effect amplified a higher hydrodynamic pressure with larger region, although the grooves located at downstream. Therefore, the reduction of wall shear stress enhanced the maximum hydrodynamic pressure in OPP.

Referring to Fig. 11(b), 11(e), 12(b), 12(e), 13(b) and 13(e), the wall shear stress for WPP was fluctuating and reaching its peak value near texture. The fluctuating wall shear stress near the texture is possibly caused by reduced fluid velocity inside the cavity, resulting in low local friction. Conversely, the wall shear stress near texture of OPP showed less fluctuating (more stable). Although the OPP generates the largest wall shear stress in regions after the minimum fluid film thickness, the wall shear stress for OPP was found to be lower in regions outside of the texture. As a matter of fact, the OPP generates lower wall shear stress compared to PB. The smoother shear profile observed in OPP contributes to its lower friction force. Similar effects were observed in both PW and CW lubrication, but the shear stress from CW lubrication is higher than PW lubrication due to its higher viscosity.

Variations in peak pressure directly affects cavitation behaviour. At high load condition (ε = 0.7, N = 1000 rpm), OPP cavities were filled with vapor, while WPP cavities contained a water–vapor mix (see Fig. 11(c) and 11(f)). The presence of vapor in OPP cavities at high eccentricity and rotational speed reduced fluid resistance, further decreasing friction due to its lower viscosity than the water.

At lower eccentricity (ε = 0.3), PW lubrication led to fully liquid cavities for both OPP and WPP due to its lower pressure peak generated. But under CW lubrication, the OPP cavities became vapor-filled while WPP cavities remained liquid (See Fig. 12(c) and 12(f)). Similarly, at low speed (N = 200 rpm), the texture cavities of both OPP and WPP were occupied by water under PW lubrication, but the texture cavities of OPP were occupied by vapour under CW lubrication (see Fig. 13(c) and 13(f)). This phenomenon can be explained by the fact that a lower eccentricity ratio generates a thicker film thickness whereas a lower speed generates a smaller pressure peak, leading to a smaller fluid film pressure peak that may prevent vaporization.

Overall, the pressure distribution is higher under CW lubrication due to higher viscosity across eccentricity ratios and rotational speeds. Besides that, OPP produced a higher peak pressure near the convergent region of HJB compared to the two other cases under both PW and CW lubrication (see Table 17 to 22). On the other hand, the pressure distribution for PB under PW and CW was discontinuous, and a complete high-pressure region was not formed at ε = 0.7 (see Table 17, 18, 21 and 22). This is because the increment of wall shear stress increased the frictional force between the bearing surface and the lubricant, which affected the lubricant flow and caused lower hydrodynamic pressure and weaker fluid film stability compared to textured HJB.

At ε = 0.3, there was no vapour formation under PW lubrication. However, wall shear stress fluctuation was observed in PB, caused by the hydrodynamic pressure gradient in the converging-diverging film region, which destabilized the local film thickness and induced shear variations along the circumferential direction. In contrast, the addition of grooves moderated these gradients, resulting in a smoother wall shear stress distribution. This is demonstrated in the added contours plots (see Table 17 to 22), comparing pressure, vapour volume fraction and wall shear stress distribution among OPP, WPP and PB across eccentricity ratios and speeds under PW and CW lubrication.

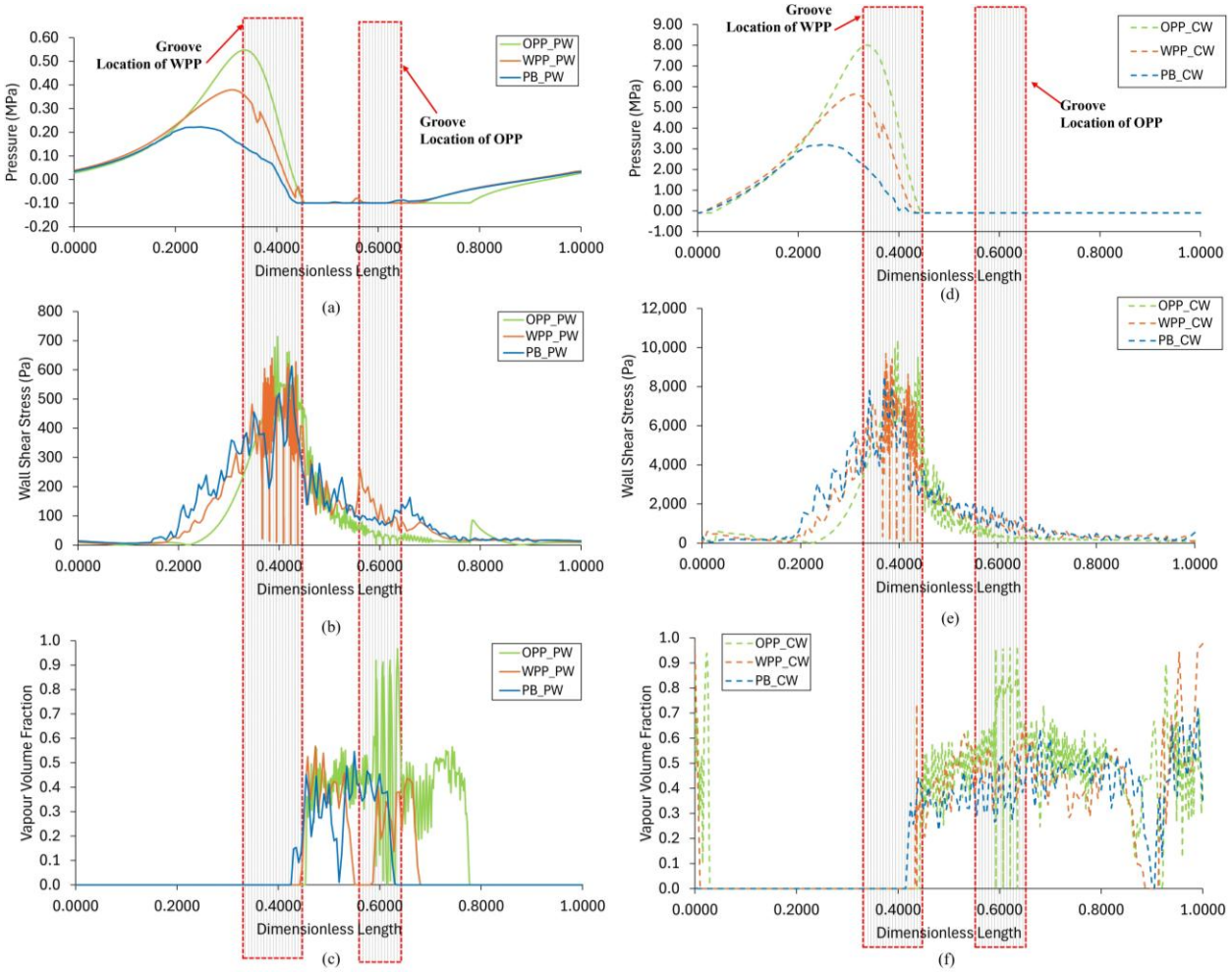

Fig. 11. Distribution plots at 0.7 eccentricity ratio and 1000 rpm for: (a) pressure, (b) wall shear stress, (c) vapour volume fraction for PW; and (d) pressure, (e) wall shear stress and (f) vapour volume fraction for CW.

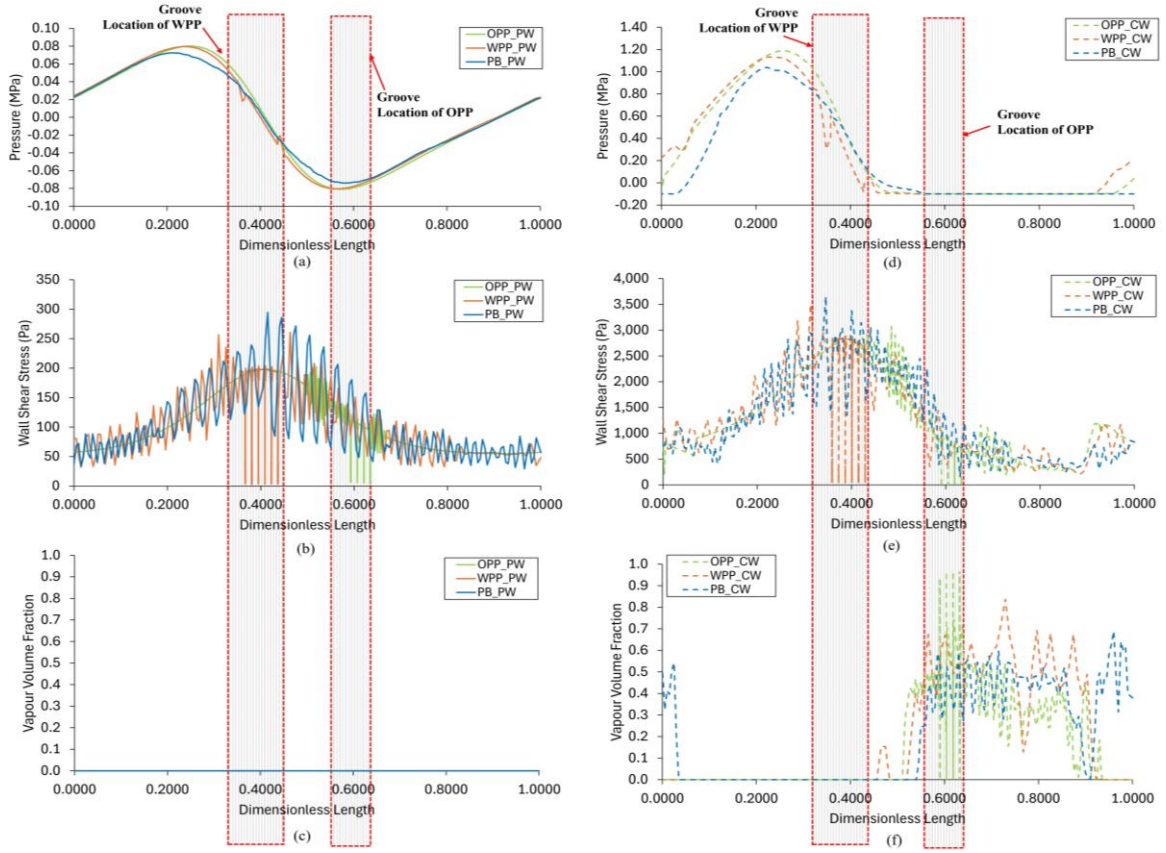

Fig. 12. Distribution plots at 0.3 eccentricity ratio and 1000 rpm for: (a) pressure, (b) wall shear stress, (c) vapour volume fraction for PW; and (d) pressure, (e) wall shear stress and (f) vapour volume fraction for CW.

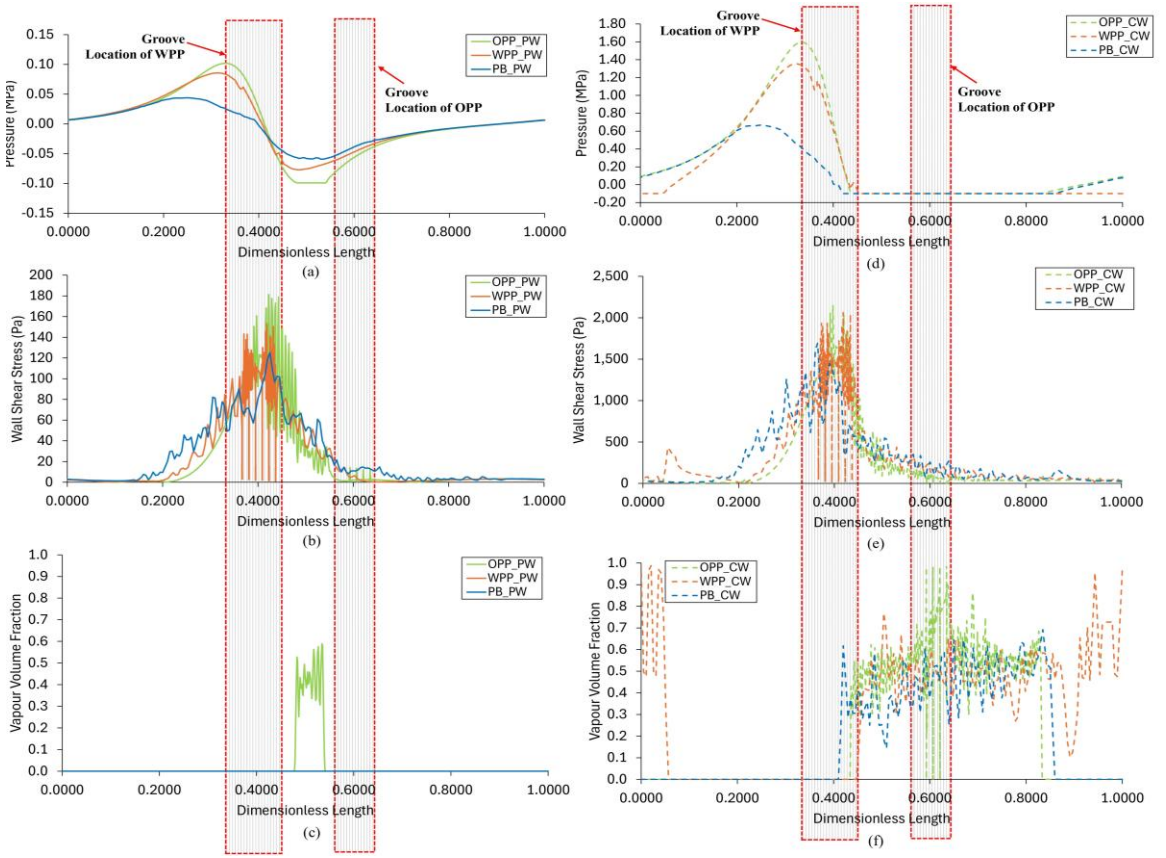

Fig. 13. Distribution plots at 0.7 eccentricity ratio and 200 rpm for: (a) pressure, (b) wall shear stress, (c) vapour volume fraction for PW; and (d) pressure, (e) wall shear stress and (f) vapour volume fraction for CW.

Table 17. Pressure, vapour volume fraction and wall shear contours at ε = 0.7, *N* = 1000 rpm under PW.

Case	Pressure	VVF	WS
OPP_ PW	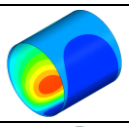	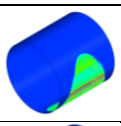	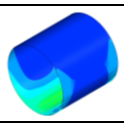
WPP _PW	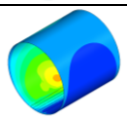	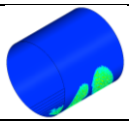	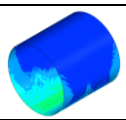
PB_ PW	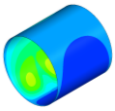	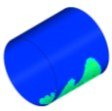	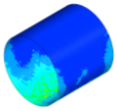
Scale	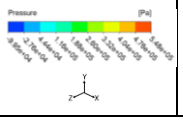	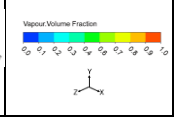	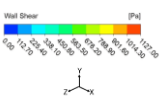

Table 18. Pressure, vapour volume fraction and wall shear contours at ε = 0.7, *N* = 1000 rpm under CW.

Case	Pressure	VVF	WS
OPP_ CW	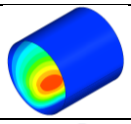	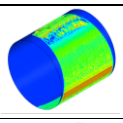	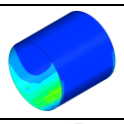
WPP _CW	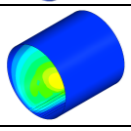	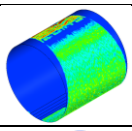	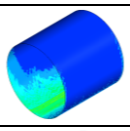
PB_ CW	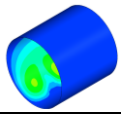	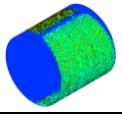	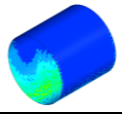
Scale	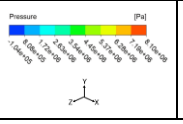	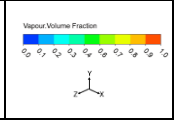	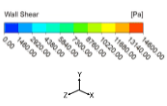

Table 19. Pressure, vapour volume fraction and wall shear contours at ε = 0.3, *N* = 1000 rpm under PW.

Case	Pressure	VVF	WS
OPP_ PW	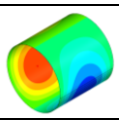	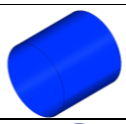	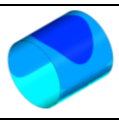
WPP _PW	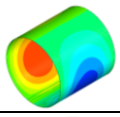	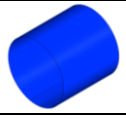	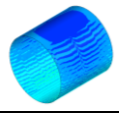
PB_ PW	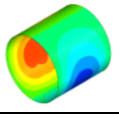	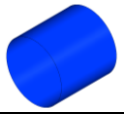	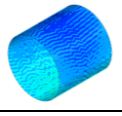
Scale	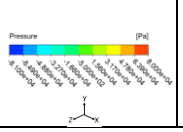	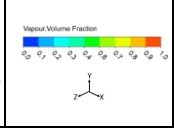	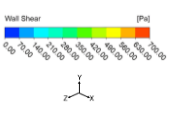

Table 20. Pressure, vapour volume fraction and wall shear contours at ε = 0.3, *N* = 1000 rpm under CW.

Case	Pressure	VVF	WS
OPP_ CW	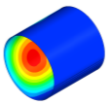	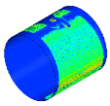	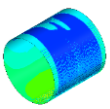
WPP _CW	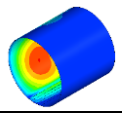	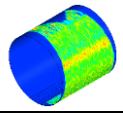	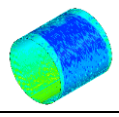
PB_ CW	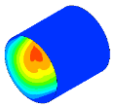	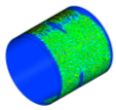	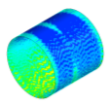
Scale	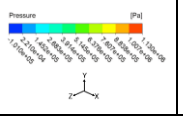	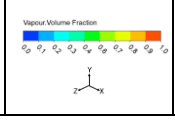	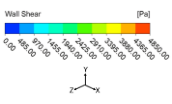

Table 21. Pressure, vapour volume fraction and wall shear contours at ε = 0.7, *N* = 200 rpm under PW.

Case	Pressure	VVF	WS
OPP_ PW	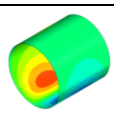	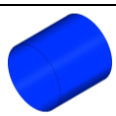	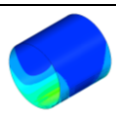
WPP _PW	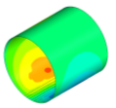	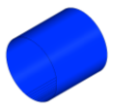	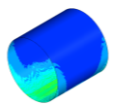
PB_ PW		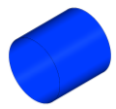	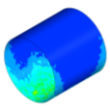
Scale	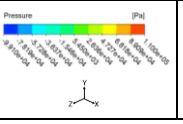	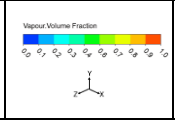	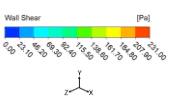

Table 22. Pressure, vapour volume fraction and wall shear contours at ε = 0.7, *N* = 200 rpm under CW.

Case	Pressure	VVF	WS
OPP_ CW	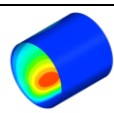	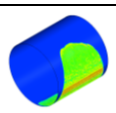	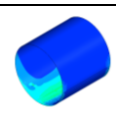
WPP _CW	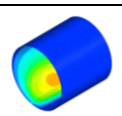	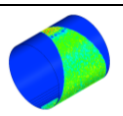	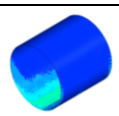
PB_ CW	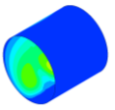	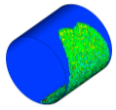	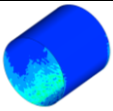
Scale	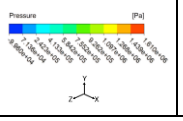	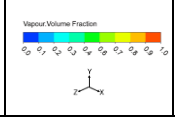	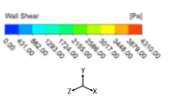

4. CONCLUSION

The performance of WLJB with rectangular grooves surface texture was analysed under pure and contaminated water lubrications across various operating conditions. The key findings of this study are summarized as follows:

1. The presence of groove textures improved WLJB performance compared to PB. Using Taguchi-based GRA, the optimal groove configuration was identified as an 80 μm groove width, four grooves and placement at θ_C. Conversely, the worst-performing configuration involved a groove width of 40 μm, six grooves and placement at θ_B.
2. Contamination provided an advantage that enhanced the performance of the optimal parameter for WLJB, where the OPP of TB under PW and CW improved LCC by 33.62% and 43.33%, respectively, while reducing friction force by 1.36% and 2.60% at ε = 0.3 and N = 1000 rpm compared to PB.
3. Groove location had the most significant effect on LCC and F_f, while groove width had the least significant effect under both of PW and CW lubrication. In ANOVA, groove location was statistically significant at the 95% of confidence level for LCC and F_f under PW and CW lubrication. Additionally, the number of grooves was statistically significant at the 95% of confidence level for F_f under CW.
4. The results also demonstrated that pressure distribution is a critical factor in improving LCC, while wall shear stress and vapour volume fraction are key indicators for reducing F_f.

This study used fixed HJB dimensions from a published paper and did not consider the actual presence of solid particles within the lubricant or the effects of temperature, which can influence lubrication mechanisms. Therefore, future work should incorporate particle and heat transfer modelling. Besides that, variations in HJB design parameters may be considered, and surface texture optimization can include groove depth and shapes, which were fixed in this study. Although no experimental validation was performed for textured bearings under CW, future work will incorporate experimental rigs to confirm CFD predictions.

Acknowledgements

The authors would like to thank Nur'Aliya Fatiha Ahmad Shahrul Nizam and Muhammad Amirul Hilmi Mazukifli for their assistance throughout the course of this work. The authors are also grateful to the Ministry of Higher Education, Malaysia, for financial support through the Fundamental Research Grant Scheme (FRGS) under project grant No. Ref: FRGS/1/2023/TK10/UTM/02/9. This work was also supported by the Universiti Teknologi Malaysia Encouragement Research (UTMER), 20J12.

REFERENCES

[1] S. Kumar, V. Kumar, and A. K. Singh, "Influence of lubricants on the performance of journal bearings – a review," *Tribology - Materials Surfaces & Interfaces*, vol. 14, no. 2, pp. 67–78, Jan. 2020, doi: 10.1080/17515831.2020.1712112.

[2] Z. Rasep, "A Study of Cavitation Effect in a Journal Bearing Using CFD: A Case Study of Engine Oil, Palm Oil and Water," *Jurnal Tribologi*, vol. 28, pp. 48–62, Mar. 2021.

[3] N. R. Chauhan, A. Khera, S. Agarwal, M. Bagri, and A. Aggarwal, "Effect of Nanoparticle on the Performance of Water Lubricated Journal Bearing," *IOP Conf Ser Mater Sci Eng*, vol. 1228, no. 1, p. 012032, Mar. 2022, doi: 10.1088/1757-899x/1228/1/012032.

[4] X. Zhang *et al.*, "Analysis of Water-Lubricated Journal Bearings Assisted by a Small Quantity of Secondary Lubricating Medium with Navier–Stokes Equation and VOF Model," *Lubricants*, vol. 12, no. 1, p. 16 Jan. 2024, doi: 10.3390/lubricants12010016.

[5] M. M. Khonsari and E. R. Booser, "Effect of Contamination on The Performance of Hydrodynamic Bearings," *Proceedings of the Institution of Mechanical Engineers Part J Journal of Engineering Tribology*, vol. 220, no. 5, pp. 419–428, May 2006, doi: 10.1243/13506501J00705.

[6] S. Poddar and N. Tandon, "Detection of Particle Contamination in Journal Bearing Using Acoustic Emission and Vibration Monitoring Techniques," *Tribology International,* vol. 134, pp. 154–164, Feb. 2019, doi: 10.1016/j.triboint.2019.01.050.

[7] G. K. Nikas, "A state-of-the-art Review on The Effects of Particulate Contamination and Related Topics in Machine-element Contacts,"

Proceedings of the Institution of Mechanical Engineers Part J Journal of Engineering Tribology, vol. 224, no. 5, pp. 453–479, Mar. 2010, doi: 10.1243/13506501JET752.

[8] H. Boucherit, B. Bou-Saïd, and M. Lahmar, "The Effect Solid Particle Lubricant Contamination on the Dynamic Behavior of Compliant Journal Bearings," *Lubrication Science*, vol. 29, no. 7, pp. 425–439, Nov. 2017, doi: 10.1002/ls.1378.

[9] P. S. Kumar *et al.*, "A Study of Surface Fatigue Wear And Influence of Contaminated Lubricant in Journal Bearing System Using Tribological And Vibration Analyses," *Proceedings of the Institution of Mechanical Engineers Part E Journal of Process Mechanical Engineering*, vol. 239, no. 6, pp. 3622–3636, Feb. 2024, doi: 10.1177/09544089241233119.

[10] W. Litwin, A. Barszczewska, E. Piątkowska, I. Szwoch, L. Matuszewski, and M. Kahsin, "Influence of Lubrication Water Contamination by Solid Particles of Mineral Origin on Marine Strut Propeller Shafts Bearings of Ships," *Polish Maritime Research*, vol. 31, no. 4, pp. 187–196, Dec. 2024, doi: 10.2478/pomr-2024-0062.

[11] S. Mishra and S. Aggarwal, "A Review of Performance of Textured Journal Bearing," *Tribology Online*, vol. 18, no. 7, pp. 494–507, Nov. 2023, doi: 10.2474/trol.18.494.

[12] P. Li, F. Zeng, S. Xiao, D. Zhen, H. Zhang, and Z. Shi, "Effects of Texture Bottom Profile on Static and Dynamic Characteristics of Journal Bearings," *Shock and Vibration*, vol. 2021, no. 1, Jan. 2021, doi: 10.1155/2021/7068744.

[13] S. Sharma, G. Jamwal, and R. K. Awasthi, "Numerical Study on Steady State Performance Enhancement of Partial Textured Hydrodynamic Journal Bearing," *Industrial Lubrication and Tribology*, vol. 71, no. 9, pp. 1055–1063, Oct. 2019, doi: 10.1108/ILT-03-2019-0083.

[14] J. Jin, X. Chen, Y. Fu, and Y. Chang, "Optimal Design of the Slip–texture on a Journal-Bearing Surface," *Industrial Lubrication and Tribology*, vol. 73, no. 2, pp. 230–237, Mar. 2021, doi: 10.1108/ILT-01-2020-0022.

[15] J. Ji, Y. Fu, and Q. Bi, "The Influence of Partially Textured Slider with Orientation Ellipse Dimples on the Behavior of Hydrodynamic Lubrication," *Industrial Lubrication and Tribology*, vol. 66, no. 2, pp. 161–167, 2014, doi: 10.1108/ILT-11-2011-0087.

[16] G. Xiang and Y. Han, "Study on the Tribo-dynamic Performances of Water-lubricated Microgroove Bearings During Start-up," *Tribology International,* vol. 151, p. 106395, Jun. 2020, doi: 10.1016/j.triboint.2020.106395.

[17] B. Manser, I. Belaidi, A. Hamrani, S. Khelladi, and F. Bakir, "Texture Shape Effects on Hydrodynamic Journal Bearing Performances Using Mass-Conserving Numerical Approach," *Tribology - Materials, Surfaces and Interfaces*, vol. 14, no. 1, pp. 33–50, Jan. 2020, doi: 10.1080/17515831.2019.1666232.

[18] N. Sharma, R. Verma, S. Sharma, and S. Kango, "Qualitative Potentials of Surface Textures and Coatings in the Performance of Fluid-film Bearings: A Critical Review," *Surface Topography Metrology and Properties,* vol. 9, no. 1, p. 013002, Jan. 2021, doi: 10.1088/2051-672X/abdda0.

[19] D. Jin, K. Xiao, G. Xiang, Y. Wang, C. Wang, and H. Jia, "A Simulation Model to Comparative Analysis The Effect of Texture Bottom Shape on Wear and Lubrication Performances for Micro-groove Water Lubricated Bearings," *Surface Topography Metrology and Properties,* vol. 9, no. 2, p. 025009, Mar. 2021, doi: 10.1088/2051-672X/abf325.

[20] M. Marian, A. Almqvist, A. Rosenkranz, and M. Fillon, "Numerical Micro-texture Optimization for Lubricated Contacts—A Critical Discussion," *Friction*, vol. 10, no. 11, pp. 1772–1809, Apr. 2022, doi: 10.1007/s40544-022-0609-6.

[21] A. Dadouche and M. J. Conlon, "Operational Performance of Textured Journal Bearings Lubricated with a Contaminated Fluid," *Tribology International*, vol. 93, pp. 377–389, Sep. 2015, doi: 10.1016/j.triboint.2015.09.022.

[22] W. Litwin, M. Wasilczuk, M. Wodtke, and A. Olszewski, "The Influence of Polymer Bearing Material and Lubricating Grooves Layout on Wear of Journal Bearings Lubricated with Contaminated Water," *Tribology International,* vol. 179, p. 108159, Dec. 2022, doi: 10.1016/j.triboint.2022.108159.

[23] W. Litwin and S. Kropp, "Sliding Bearings with Sintered Bronze Bush Lubricated by Contaminated Water with Solid Particles – Theoretical and Experimental Studies," *Wear*, vol. 532–533, p. 205070, Jul. 2023, doi: 10.1016/j.wear.2023.205070.

[24] A. B. Shinde and P. M. Pawar, "Multi-objective Optimization of Surface Textured Journal Bearing by Taguchi based Grey Relational Analysis," *Tribology International,* vol. 114, pp. 349–357, Apr. 2017, doi: 10.1016/j.triboint.2017.04.041.

[25] C. Liu, N. Zhong, X. Lu, and B. Zhao, "A Multiobjective Optimization of Journal Bearing with Double Parabolic Profiles and Groove Textures Under Steady Operating Conditions," *Mechanics and Industry*, vol. 21, no. 3, p. 305, Jan. 2020, doi: 10.1051/meca/2020017.

[26] A. Ganesha *et al.*, "Performance Optimization of a Multi-groove Water Lubricated Journal Bearing with Partial Slip by Taguchi Analysis," *Arabian Journal for Science and Engineering*, vol. 49, no. 2, pp. 2249–2267, Aug. 2023, doi: 10.1007/s13369-023-08191-z.

[27] Manish Kumar and K. N. Pandey, "Enhancing Journal Bearing Performance Through Surface Texturing: A Comprehensive Review of Latest Developments and Future Prospects," *Proceedings of the Institution of Mechanical Engineers, Part E: Journal of Process Mechanical Engineering*, vol. 239, no. 5, pp. 3062–3078, Nov. 2023, doi: 10.1177/09544089231211230.

[28] Y. Han and Y. Fu, "Comparison of Hydrodynamic Characteristics Between Circumferential and Transversal Micro-grooved Journal Bearings," *Lubrication Science*, vol. 31, no. 7, pp. 285–298, Jul. 2019, doi: 10.1002/ls.1471.

[29] G. Gao, Z. Yin, D. Jiang, and X. Zhang, "Numerical Analysis of Plain Journal Bearing Under Hydrodynamic Lubrication by Water," *Tribology International*, vol. 75, pp. 31–38, Mar. 2014, doi: 10.1016/j.triboint.2014.03.009.

[30] T. Liu *et al.*, "Viscous Oil Film Thermal Modeling of Hydrostatic Bearings With a Rectangular Microgroove Surface," *Frontiers in Energy Research*, vol. 10, Apr. 2022, doi: 10.3389/fenrg.2022.891380.

[31] C. C. Wang and J. T. Lin, "Numerical Study of Hydrodynamic Herringbone-grooved Journal Bearings Combined with Thrust Bearings Considering Thermal Effects," *Journal of Mechanics*, vol. 38, pp. 13–21, Jan. 2022, doi: 10.1093/jom/ufab036.

[32] Z. Rasep, M. N. A. W. M. Yazid, S. Samion, and N. A. C. Sidik, "Potential of RBD Palm Oil as a Lubricant in Textured Journal Bearing using CFD with Consideration of Cavitation and Conjugate Heat Transfer," *CFD Letters*, vol. 14, no. 2, pp. 98–110, Feb. 2022, doi: 10.37934/cfdl.14.2.98110.

[33] S. Kango, R. K. Sharma, and R. K. Pandey, "Comparative Analysis of Textured and Grooved Hydrodynamic Journal Bearing," *Proceedings of the Institution of Mechanical Engineers, Part J: Journal of Engineering Tribology*, vol. 228, no. 1, pp. 82–95, Aug. 2013, doi: 10.1177/1350650113499742.

[34] Z. Rasep, M. N. A. W. M. Yazid, and S. Samion, "Lubrication of Textured Journal Bearing by Using Vegetable Oil: A Review of Approaches, Challenges, And Opportunities," *Renewable and Sustainable Energy Reviews*, vol. 146, p. 111191, May 2021, doi: 10.1016/j.rser.2021.111191.

[35] D. Y. Dhande and D. W. Pande, "Multiphase Flow Analysis of Hydrodynamic Journal Bearing Using CFD Coupled Fluid Structure Interaction Considering Cavitation," *Journal of King Saud University - Engineering Sciences*, vol. 30, no. 4, pp. 345–354, Oct. 2018, doi: 10.1016/j.jksues.2016.09.001.

[36] G. Ou, P. Ouyang, Z. Zheng, H. Jin, K. Bie, and C. Wang, "Investigation on Failure Process and Structural Improvement of A High-pressure Coal Water Slurry Valve," *Engineering Failure Analysis,* vol. 96, pp. 1–17, Sep. 2018, doi: 10.1016/j.engfailanal.2018.09.003.

[37] M. Rakibuzzaman, H. H. Kim, K. Kim, S. H. Suh, and K. Y. Kim, "Numerical Study of Sediment Erosion Analysis in Francis Turbine," *Sustainability (Switzerland)*, vol. 11, no. 5, p. 1423, Mar. 2019, doi: 10.3390/su11051423.

[38] Z. Yang, G. Yu, and Q. Zhao, "Experimental Study and Numerical Simulation of Sediment's Promoting Effect on Cavitation Based on Flow Field Analysis," *Processes*, vol. 13, no. 5, p. 1299, May 2025, doi: 10.3390/pr13051299.

[39] Y. Zhou, X. Shi, Y. Chen, L. Wang, and C. Chen, "Hydrodynamic Analysis of Journal Bearing Considering The Effects of Cavitation And Minuscule Particle," *Journal of Physics Conference Series*, vol. 2599, no. 1, p. 012047, Sep. 2023, doi: 10.1088/1742-6596/2599/1/012047.

[40] Z. Xie *et al.*, "Fluid-structure Interaction Analysis of A Novel Water-lubricated Bearing with Particle-dynamic Effect: Theory and Experiment," *Tribology International*, vol. 204, p. 110474 Dec. 2024, doi: 10.1016/j.triboint.2024.110474.

[41] A. A. Minea, "Hybrid Nanofluids Based on Al2O3, TiO2 and SiO2: Numerical Evaluation of Different Approaches," *International Journal of Heat and Mass Transfer*, vol. 104, pp. 852–860, Jan. 2017, doi: 10.1016/j.ijheatmasstransfer.2016.09.012.

[42] F. M. Meng, L. Zhang, Y. Liu, and T. T. Li, "Effect of Compound Dimple on Tribological Performances of Journal Bearing," *Tribology International*, vol. 91, pp. 99–110, Jul. 2015, doi: 10.1016/j.triboint.2015.06.030.

[43] M. Malki, S. Larbi, S. Boubendir, and R. Bennacer, "Lubricant Rheological Behavior Effect Analysis on The Performance of Finite Porous Self- lubricating Journal Bearings," *Journal of Applied Fluid Mechanics*, vol. 11, no. 6, pp. 1557–1568, 2018, doi: 10.29252/jafm.11.06.28883.

[44] Q. Li, Y. Wang, X. Li, G. Zhang, Y. Du, and W. Xu, "Investigation and Optimization of Textured Water-lubricated Journal Bearings Using Multi-objective Optimization," *Journal of Applied Fluid Mechanics*, vol. 17, no. 9, pp. 1912–1928, Jul. 2024, doi: 10.47176/jafm.17.9.2581.

[45] P. Jayaraman and L. Mahesh Kumar, "Multi-response Optimization of Machining Parameters of Turning AA6063 T6 Aluminium Alloy Using Grey Relational Analysis in Taguchi Method," *Procedia Engineering*, vol. 97, pp. 197–204, Jan. 2014, doi: 10.1016/j.proeng.2014.12.242.

[46] M. Gawkhare, "Grey Relation Analysis Methodology and Its Application," *RESEARCH REVIEW International Journal of Multidisciplinary*, vol. 4, no. 2, pp. 409–411, Feb. 2019, doi: 10.5281/zenodo.2578088.